Hindawi
Shock and Vibration
Volume 2024, Article ID 6666054, 17 pages
https://doi.org/10.1155/2024/6666054

Research Article

Efficient Dynamic Performance Prediction of Railway Bridges Situated on Small-Radius Reverse Curves

Yumin Song,[1,2] **Bin Hu**,[1] **and Xiaoliang Meng**[1]

[1]*School of Urban Rail Transportation, Shanghai University of Engineering Science, Shanghai 201620, China*
[2]*State Key Laboratory of Bridge Engineering Structural Dynamics and Key Laboratory of Bridge Earthquake Resistance Technology, Ministry of Communications, Chongqing 400067, China*

Correspondence should be addressed to Yumin Song; song-yumin@qq.com

Received 20 November 2023; Revised 20 February 2024; Accepted 9 March 2024; Published 9 April 2024

Academic Editor: Nicolo Zampieri

Bridges situated on small-radius reverse curves play a pivotal role within some railway networks, exerting influence over project-wide design progress. Typically, assessing the safety of bridge design parameters necessitates laborious vehicle-bridge dynamic coupling vibration numerical analysis or model experiments. To streamline the design process and enhance efficiency during the preliminary design phase, we propose an efficient method to assess the dynamic performance of bridges on small-radius reverse curves. This approach enables direct prediction of bridge dynamic performance based on design parameters, eliminating the need for numerical simulations and model experiments. We first develop a vehicle-bridge coupling vibration program grounded in train-curve bridge coupling vibration theory, validated using on-site measured data. Subsequently, through numerical simulation experiments, we evaluate 80 simply supported beam bridges on small-radius reverse curves under various operating conditions, generating ample dynamic response data for bridge pier tops and girders. These data are then compared with regulatory thresholds to assign dynamic performance labels. After identifying essential design parameters as data features using Fisher scores, we proceed to input these features into a support vector machine (SVM). Through supervised training with dynamic performance labels, this process empowers the SVM model to predict the dynamic performance of the bridge. Our results demonstrate that this method circumvents the need for detailed vehicle-bridge interaction analysis, yielding an impressive 86.9% accuracy in predicting dynamic performance and significantly boosting computational efficiency. Besides, the top five design parameters that significantly influence the prediction of bridge dynamic performance are obtained. This novel approach has the potential to expedite design assessments and enhance safety in railway bridge construction.

1. Introduction

Bridges situated on small-radius reverse curves hold a pivotal role in railway networks, shaping project design progress. Traditionally, ensuring the safety of these bridge design parameters involves time-consuming vehicle-bridge dynamic coupling vibration numerical analysis and model experiments.

Over the past decades, the dynamic interaction between moving vehicles and bridges has been extensively studied. Researchers have employed various numerical models and analysis methods to address vehicle-bridge interaction. These studies contribute to structural dynamics and encompass theoretical, numerical simulation, and real-world experimental aspects [1–5]. These investigations often utilize different vehicle models, such as moving force models, moving mass models, quarter-vehicle models, and full-vehicle models [6–15]. These models describe vehicle motion and response through theoretical deduction or finite element modeling. Simultaneously, numerical simulation of bridge structures usually employs finite element modeling to account for their intricate structural attributes. The vehicle-bridge interaction (VBI) system, a core concept in this field, describes the dynamic interaction between vehicles and bridges [16, 17]. This system models vehicle and bridge subsystems while considering wheel-rail contact interactions. The VBI system models, through theoretical analysis or numerical simulation, have demonstrated

accurate simulations of vehicle and bridge dynamic responses. However, in some cases, considering the full-vehicle model and spatial dynamic interaction can entail high computational costs, particularly when extensive simulations or real-time online evaluations are required [2, 18, 19].

Recently, machine learning methods have emerged as promising computational algorithms in civil structural dynamics. Machine learning models demonstrate the ability to tackle complex structural dynamic challenges by leveraging vast structural data and vibrational information, providing efficient and accurate predictions. Notably, literature [20, 21] employed fully connected neural networks for dynamic analysis of buildings under seismic excitations, reducing computational workload. Another study [22] predicted wind pressure time histories for tall buildings using machine learning, addressing the dynamic effects of wind loads. In addition, references [23, 24] estimated aerodynamic forces and responses for long-span bridges, exploring deep learning algorithms for dynamic response prediction of wind-sensitive structures. In the realm of predicting vehicle-bridge interaction, reference [25] developed an artificial neural network as a proxy model for VBI systems in railway transportation, aiming to predict the time history of bridge responses caused by vehicles. Furthermore, reference [26] employed a nonlinear autoregressive exogenous input neural network model to predict bridge accelerations subjected to quarter-vehicle model loads in the vertical plane. Beyond time history estimation, machine learning methods have been employed to predict statistical variables. Reference [27] achieved maximum response prediction of building structures under artificial seismic effects using structural parameters and multilayer perceptrons. Reference [28] predicted the average strain response of bridges by selecting total vehicle weight, truck length, vehicle speed, and truck axle spacing as neural network inputs. However, to the author's knowledge, no literature has been found that utilizes a machine learning approach to directly predict the dynamic performance of bridges on small-radius curves subjected to vehicle-induced vibrations and assess the importance of selected design parameters for the dynamic performance prediction.

The objective of this paper is to propose an efficient method for predicting the dynamic performance of bridges on small-radius reverse curves, bypassing the cumbersome steps of numerical simulation or model experiments, and enhancing bridge design efficiency. The main process of the methodology proposed in this article is described in Figure 1. First, we establish a vehicle-bridge coupling vibration program based on train-curve bridge coupling vibration theory and validate it using on-site measured data. Subsequently, we conduct numerical simulation experiments on 80 simply supported beam bridges located on small-radius reverse curves under various operating conditions, generating ample dynamic response data for bridge pier tops and girders. This data is then compared with regulatory thresholds to assign dynamic performance labels. By selecting critical bridge design parameters as data features, we input them into a support vector machine (SVM) and train the model under the supervision of dynamic performance labels, empowering the SVM model with the ability to predict the dynamic performance of bridge piers and girders. In conclusion, our proposed approach offers a novel and efficient method to predict the dynamic performance of bridges on small-radius reverse curves, alleviating the need for exhaustive numerical simulations or model experiments. This methodology holds the potential to accelerate design assessments and enhance safety in railway bridge construction.

2. Vehicle-Curve Bridge Coupling Vibration Model

2.1. Model Construction. The interaction system between the vehicle and the bridge is comprised of two subsystems: the vehicle subsystem and the bridge subsystem. These two subsystems are connected through wheel-rail interactions, with irregularities in the given track serving as an additional excitation for the system. The two subsystems utilize a common coordinate system where the x-axis aligns with the direction of train travel, the y-axis points upward, and the z-axis is defined according to the right-hand rule. This study employs the modal superposition method [29] to solve the coupled vehicle-bridge vibration equation. The implementation encompasses both program development and the incorporation of modal analysis results obtained from the commercial software ANSYS. Subsequent sections provide an introduction to the spatial relationships of the vehicle and curved bridge in modal coordinates, as well as an explanation of the coupled vibration equations.

2.1.1. Train-Curved Bridge Spatial Relationship Processing. Utilizing the method of moving coordinates and employing coordinate transformations, the precise position of a train as it traverses a curved bridge at a specific moment can be ascertained. The mobile coordinate system is tailored for each wheelset and moves uniformly along the centerline of the track. The origin of this coordinate system is situated at the intersection point of the wheel axle and the track centerline. According to the right-hand rule, the positive direction of the x-axis aligns with the tangent to the curve, the positive direction of the y-axis points vertically upwards from the track plane, and the positive direction of the z-axis corresponds to the curve's normal direction. This is depicted in the coordinate systems denoted as $o_i x_i y_i z_i$ and $o_j x_j y_j z_j$, as illustrated in Figure 2.

Assuming the train is moving at a constant velocity, denoted as v, and at time t, the train has covered a distance of S_i along the track. By considering the characteristics of the track curvature, the pertinent parameters at point S_i (representing the train's position at time t) can be determined:

(1) The overall coordinates of the curve represented as (X_{Oi}, Y_{Oi}, Z_{Oi});

(2) Parameters at point S_i including the angle α_i between the curve's tangent and the OX axis, curvature ρ_i, and cant angle γ_i;

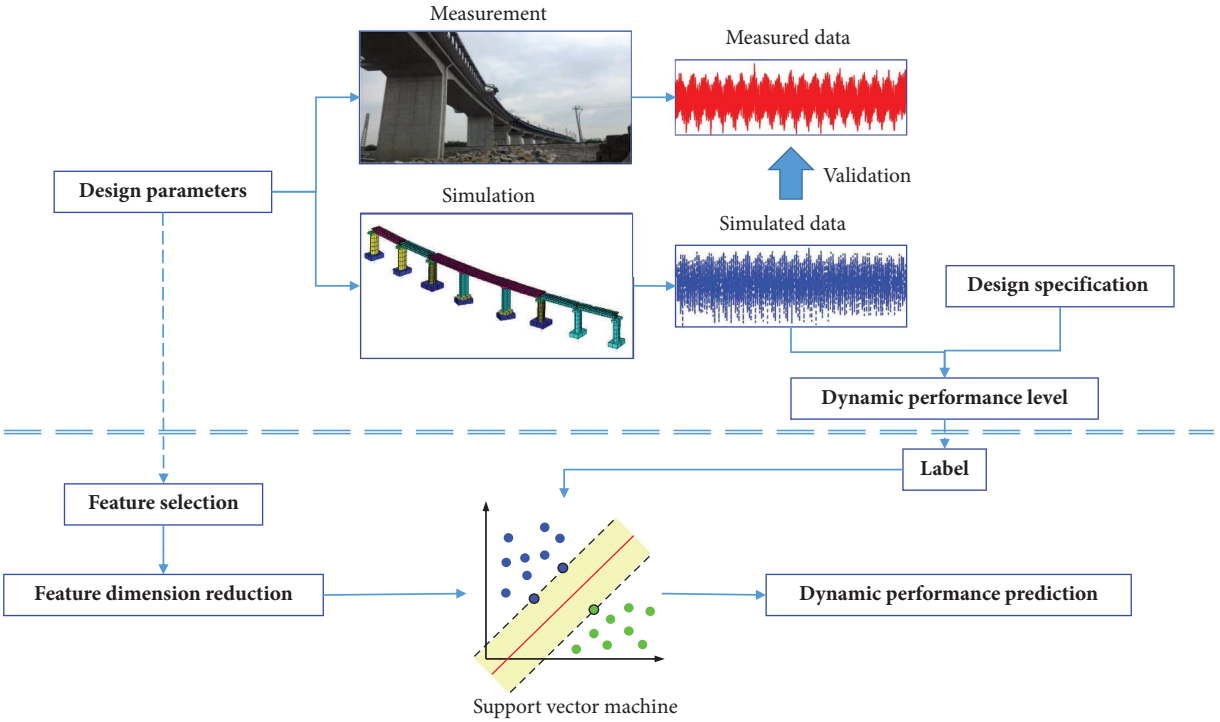

Figure 1: Main process of the methodology.

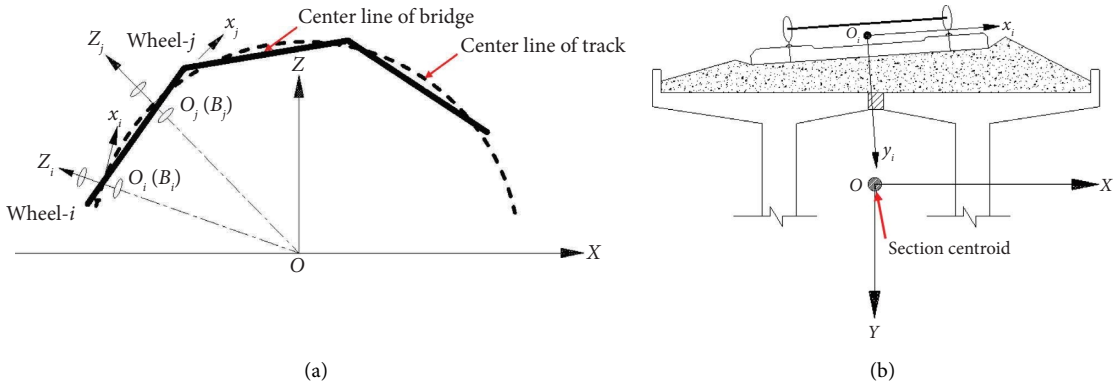

Figure 2: Moving coordinate of vehicle-curved bridge system. (a) Plan. (b) Front view.

(3) The employed moving coordinate systems, $o_i x_i y_i z_i$ and $o_j x_j y_j z_j$.

Assuming the wheelset's center plane projection at time t coincides with the centroid line of the bridge at node B_i, the transformation expression of the kth mode shape vector φ from the global coordinate system $OXYZ$ to the moving coordinate system $o_i x_i y_i z_i$ can be formulated as follows:

$$\varphi_{i,B} = \lambda\varphi = \begin{bmatrix} \Lambda & 0 \\ 0 & \Lambda \end{bmatrix}\varphi. \tag{1}$$

In the provided equation, $\varphi_{i,B}$ denotes the displacement vector of the bridge's centroid mode shape in the moving coordinate system. The matrix λ represents the coordinate transformation matrix, attainable through a sequence of two coordinate rotations.

The formulation for Λ is given by

$$\Lambda = \begin{bmatrix} \cos\alpha_i & 0 & \sin\alpha_i \\ -\sin\alpha_i \sin\gamma_i & \cos\gamma_i & \cos\alpha_i \sin\gamma_i \\ -\sin\alpha_i \sin\gamma_i & -\sin\gamma_i & \cos\alpha_i \cos\gamma_i \end{bmatrix}. \tag{2}$$

After the coordinate transformation, the mode shape vector $\varphi_{i,B}$ centered around the bridge's centroid requires additional contemplation of the rigid arm constraint equations. When transitioning to the point along the track with a distance S_i where the train is situated, the vector φ_i undergoes a transformation characterized by the following relationship:

$$\begin{Bmatrix} x_{i,B} + S_i \\ y_{i,B} \\ z_{i,B} \end{Bmatrix} = \Lambda \begin{Bmatrix} x_{Bi} - x_{Oi} \\ y_{Bi} - y_{Oi} \\ z_{Bi} - z_{Oi} \end{Bmatrix} + \begin{Bmatrix} S_i \\ 0 \\ 0 \end{Bmatrix},$$
$$\varphi_i = \begin{bmatrix} 1 & 0 & 0 & 0 & 0 & 0 \\ 0 & 1 & 0 & z_{i,B} & 0 & 0 \\ 0 & 0 & 1 & -y_{i,B} & 0 & 0 \\ 0 & 0 & 0 & 1 & 0 & 0 \\ 0 & 0 & 0 & 0 & 1 & 0 \\ 0 & 0 & 0 & 0 & 0 & 1 \end{bmatrix} \varphi_{i,B}. \tag{3}$$

In the equation, $x_{i,B}$, $y_{i,B}$, and $z_{i,B}$ denote the positional coordinates of the bridge centroid node B_i in the moving coordinate system.

If at time t the plane projection of the wheelset center does not coincide with the bridge centroid node B_i, a solution can be achieved by utilizing a third-order cubic spline interpolation between the overlapping points. This approach allows for the determination of the bridge's mode shape displacement at any given point along the track's centerline.

2.1.2. Train-Curved Bridge Coupling Vibration Equation. Using the modal superposition technique [30], the dynamic differential equations of the coupled vehicle-bridge vibration system are established. This methodology involves segregating the vibration system into distinct vehicle and bridge subsystems. The resultant set of differential equations governing the overall system's motion is articulated as follows:

$$\begin{cases} \{\ddot{q}_v\} + 2[\xi_v][\omega_v]\{\dot{q}_v\} + [\omega_v^2]\{q_v\} = \{f_v(\{q_v\}, \{\dot{q}_v\}, \{\ddot{q}_v\}, \{q_b\}, \{\dot{q}_b\}, \{\ddot{q}_b\})\}, \\ \{\ddot{q}_b\} + 2[\xi_b][\omega_b]\{\dot{q}_b\} + [\omega_b^2]\{q_b\} = \{f_b(\{q_v\}, \{\dot{q}_v\}, \{\ddot{q}_v\}, \{q_b\}, \{\dot{q}_b\}, \{\ddot{q}_b\})\}, \end{cases} \tag{4}$$

where subscripts v and b, respectively, pertain to the vehicle and the bridge.

The dynamic interaction between the train and the bridge is realized by means of the coupling forces exerted at the contact interface between the two subsystems. These coupling forces serve as the mechanism for coupling and simultaneously act as internal excitations within the vibration system. Conversely, generalized forces represent external excitations applied to the vibration system.

(1) Solving Wheel-Rail Contact Force. The contact forces at the wheel-rail interface for both the vehicle and bridge subsystems represent critical boundary conditions. Under spatial vibration conditions, these contact forces consist of the vertical force F_{yj} and the lateral force F_{zj} acting at the wheel-rail interface. Exploiting the assumptions of tight wheel-rail contact and neglecting yaw angles (assuming that the wheelset is always in radial position), the association between each contact force and the respective normal force N_j and tangential force T_{zj} in the coordinate system established at the contact point is formulated as follows:

$$\begin{cases} F_{y1} = N_1 \cos(\delta_1 + \theta_{ws}) - T_{z1} \sin(\delta_1 + \theta_{ws}), \\ F_{z1} = N_1 \sin(\delta_1 + \theta_{ws}) + T_{z1} \cos(\delta_1 + \theta_{ws}), \\ F_{y2} = N_2 \cos(\delta_1 - \theta_{ws}) + T_{z2} \sin(\delta_1 - \theta_{ws}), \\ F_{z2} = -N_2 \sin(\delta_1 - \theta_{ws}) + T_{z2} \cos(\delta_1 - \theta_{ws}), \end{cases} \tag{5}$$

where θ_{ws} represents the roll angle of wheelset.

(2) Calculation of Wheel-Rail Creep Force. Based on Kalker's theory of creep forces, the relationship between creep force, creep coefficient, and creepage rate is defined as follows [11]:

$$\begin{cases} T_{xj} = -f_{11j}\xi_{1j}, \\ T_{zj} = -f_{22j}\xi_{2j} + f_{23j}\xi_{3j}, \\ M_j = -f_{23j}\xi_{2j} - f_{33j}\xi_{3j}, \end{cases} \tag{6}$$

where T_{xj}, T_{zj}, and M_j represent the longitudinal creep force, lateral creep force, and rotational creep torque at the wheel-rail interface, respectively. f_{11j}, f_{22j}, f_{23j}, f_{33j} are the creep coefficients. ξ_{1j}, ξ_{2j}, and ξ_{3j} denote the longitudinal creepage rate, lateral creepage rate, and spin creepage rate of the wheel-rail contact, respectively, when the train is in straight-line motion.

The wheel-rail creepage rate for wheelsets traversing curved tracks can be revised as follows:

$$\begin{cases} \xi'_{1j} = \xi_{1j} + (-1)^j \left[-b + r_j \sin(\delta_j) \cos(\delta_j) \cos(\psi_{ws})\right] \cdot \rho_i, \\ \xi'_{2j} = \xi_{2j}, \\ \xi'_{3j} = \xi_{3j} + (-1)^j \cos(\delta_j) \cdot \rho_i, \end{cases} \tag{7}$$

where ξ'_{1j}, ξ'_{2j}, and ξ'_{3j} denote the longitudinal, lateral, and spin creepage rates of the wheel-rail contact when the wheelset traverses a curve with curvature ρ_i. r_j stands for the actual rolling radius of the wheelset. δ_j represents the wheelset contact angle. ψ_{ws} represents the wheelset yaw angle.

The influence of curvature on the creep coefficient is minimal, and for the sake of simplicity, it is often treated as if in a straight-line scenario. This treatment only considers the effect of the lateral offset of the wheelset from the track centerline when the wheelset traverses a curve.

As a result, when a vehicle undergoes uniform curved motion, the creep force at the wheel-rail interface can be expressed as follows:

$$\begin{cases} T_{xj} = -f_{11j}\xi'_{1j}, \\ T_{zj} = -f_{22j}\xi'_{2j} + f_{23j}\xi'_{3j}, \\ M_j = -f_{23j}\xi'_{2j} - f_{33j}\xi'_{3j}. \end{cases} \tag{8}$$

(3) Generalized Forces. In theory, when a train is in curved motion, the primary suspension force and secondary suspension force of the train body should be transformed into the moving coordinate system through coordinate transformations. For this study, assuming a minimum curve radius of 400 m, it can be inferred that the deviation angle between the train body coordinate system and the wheelset coordinate system is extremely small. Therefore, the calculation of primary and secondary suspension forces can be directly performed as if the train is moving in a straight line.

Centrifugal force and canting force are generalized forces that must be considered during curved train motion. Assuming the wheelset i is at a curvature of ρ_i and a cant angle of γ_i, the centrifugal force and canting force experienced by the wheelset in the moving coordinate system are as follows:

$$\begin{cases} C_{wi} = -m_{wi}\rho_i v^2, \\ H_{wi} = m_{wi} g \sin\gamma_i, \\ V_{wi} = m_{wi} g (1 - \cos\gamma_i), \end{cases} \tag{9}$$

where C_{wi} represents the centrifugal force along the o_{iz} direction. H_{wi} signifies the force along the o_{iz} direction induced by canting. V_{wi} denotes the force along the o_{iy} direction induced by canting. m_{wi} refers to the mass of the wheelset i.

Approximating by considering the average curvature and cant angle for each of the four wheelsets in a train section, the centrifugal force and canting force experienced by each train section are calculated as follows:

$$\begin{cases} C_{f,c} = -m_{f,c}\left(\dfrac{1}{4}\displaystyle\sum_{i=1}^{4}\rho_i\right)v^2, \\ H_{f,c} = m_{f,c} g \sin\left(\dfrac{1}{4}\displaystyle\sum_{i=1}^{4}\gamma_i\right), \\ V_{f,c} = m_{f,c} g\left[1 - \cos\left(\dfrac{1}{4}\displaystyle\sum_{i=1}^{4}\gamma_i\right)\right], \end{cases} \tag{10}$$

where subscripts f and c, respectively, indicate the bogie and carbody.

2.2. Model Verification

2.2.1. Field Experiment. Due to geographical constraints, a cluster of railway bridges is situated along an "*S*"-shaped curve with relatively small radii. Figure 3 illustrates the plan layout of the railway route situated in East China, depicting curve radii of 400 m, 500 m, and 500 m. Transition curves of lengths 50 m, 40 m, and 60 m are respectively used between three sections of circular arc curves. The visual representation of the railway line and bridges can be found in Figure 4. The bridge types encompass: (1) 80 prestressed concrete simply supported beam bridges: Spans include 16 m, 20 m, 24 m, and 32 m. (2) Reinforced concrete continuous rigid frame bridges: Span configurations of 18.3 + 24.0 + 18.3 m and 17.3 + 30 + 30 + 19.3 m. This study exclusively focuses on the investigation of the 80 simply supported beam bridges.

We selected several representative bridges on the railway line and installed velocity and displacement sensors at the mid-span and the top of the bridge piers. The sensors were set to a sampling frequency of 50 Hz. The layout of the sensors is illustrated in Figures 5 and 6. The predominant train types on this route are C62 freight trains [31]. The dynamic responses of the bridges as the trains passed the sensor locations were recorded.

After completing the testing phase, we performed postprocessing and concise analysis of the test signals, primarily focused on determining the resonant frequencies of the main beam and bridge piers. Figure 7 displays the displacement curve of a specific pier within 10 seconds after a train passes, along with its frequency spectrum representation. The displacement curve is measured by the displacement gauge at the top of the pier. The frequency spectrum is obtained through Fourier transform. The spectrum analysis reveals a first transverse vibration frequency of 3.6 Hz for the pier. Following this method, the resonant frequencies of both main beams and bridge piers for all tested bridges were determined.

2.2.2. Numerical Simulation. In general, employing solid elements for bridge modeling provides a finer analysis of vehicle-bridge coupling vibrations. However, given the extensive number of bridges in this case study and the focus on dynamic responses at bridge midspans and pier tops, a beam element approach was adopted for bridge modeling. The use of beam elements offers a substantial reduction in computational costs while still meeting research requirements. Figure 8 depicts the beam element finite element models for all bridges located on the *S*-shaped curve, along with the first-order vertical bending mode and first-order transverse bending mode for the 32 m bridge. With the bridge models in place, we proceeded to conduct vehicle-bridge coupling vibration analysis, following the principles outlined in Section 2.1. Given the limited data on track irregularities, the

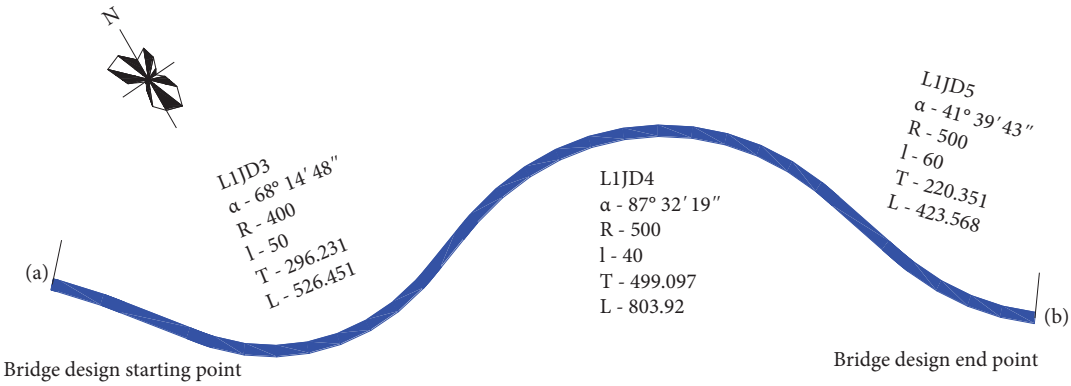

Figure 3: Plan layout of the railway line.

Figure 4: Railway line and bridge appearance. (a) Railway line. (b) Bridge.

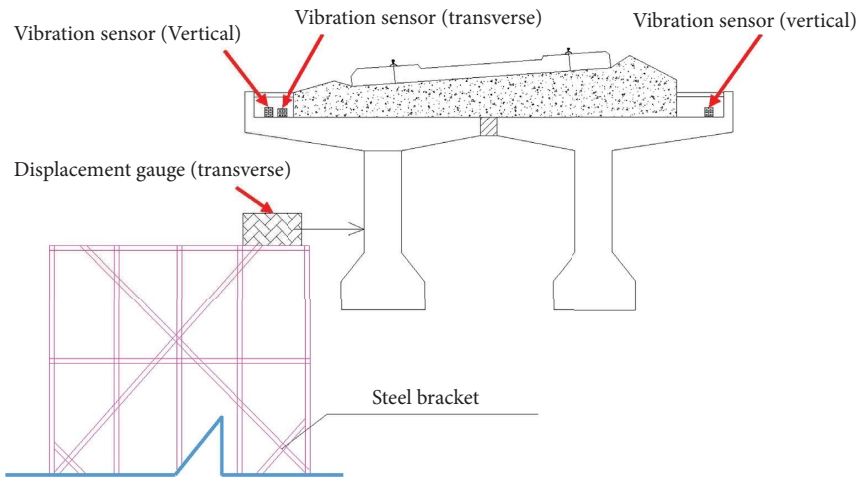

Figure 5: Arrangement of mid-span test points.

US six-level spectrum from the Federal Railroad Administration is utilized to simulate irregularities in the lateral, rotational, and vertical directions. We chose the level 5 irregularity as the track irregularity used in simulation by survey and trail. This enabled us to obtain dynamic response results for the bridge finite element models corresponding to the field test measurement points.

2.2.3. Results Comparison. We utilized displacement and velocity signals obtained from field measurements to calculate the natural frequencies of the main beam and the modal displacement ratios between the pier top and bottom. These results were then compared with the outcomes of a numerical simulation using a finite element model of the bridge. Table 1 presents a comparison between the numerical

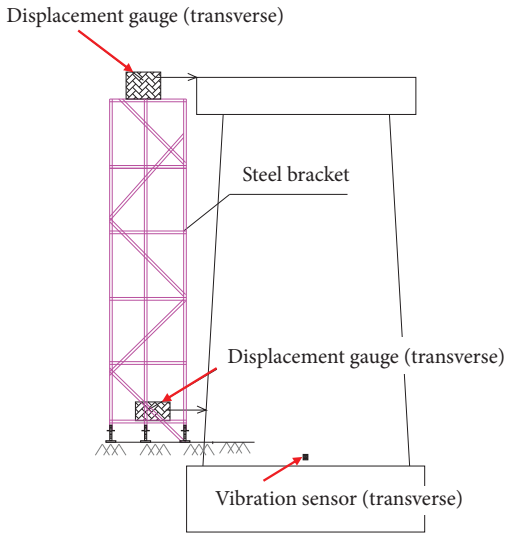

Figure 6: Arrangement of pier test points.

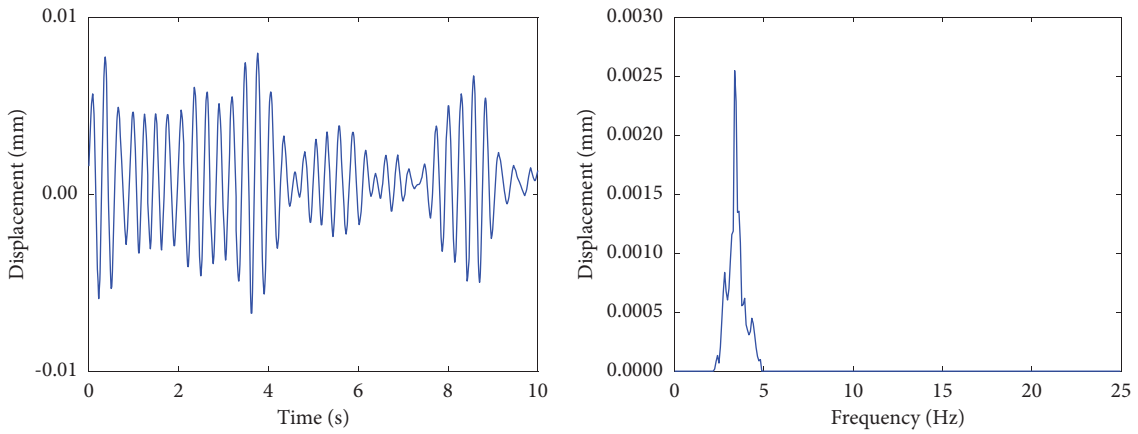

Figure 7: Residual vibration curve in time and frequency domain. (a) Time domain. (b) Frequency domain.

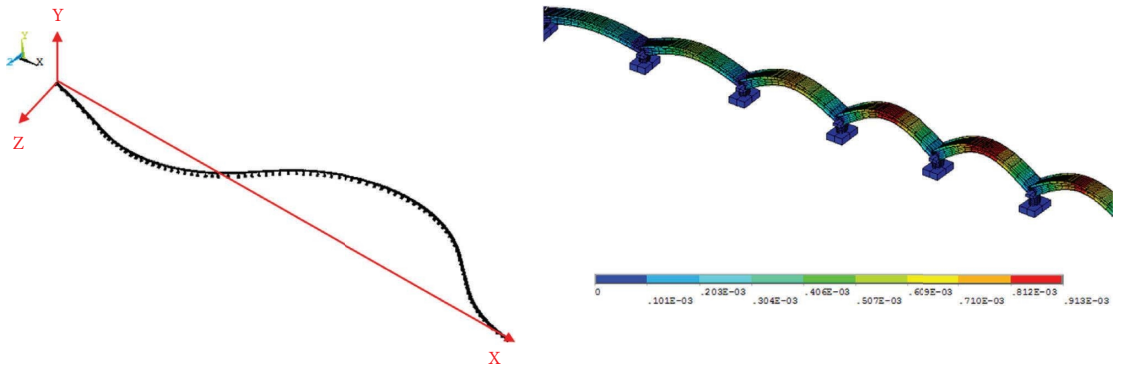

Figure 8: Continued.

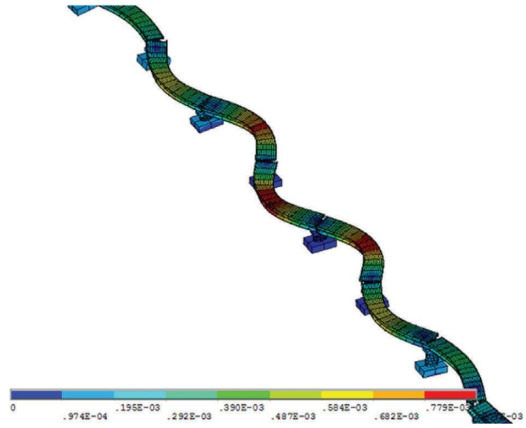

(c)

Figure 8: Bridge finite element models and typical displacement modes. (a) Finite element models of all bridges. (b) First-order vertical bending mode. (c) First-order lateral bending mode.

simulation and measured results for two bridges with spans of 20 m and 24 m. It is evident from the table that the first-order lateral natural frequencies of the main beam and the modal displacement results of the piers obtained from field measurements and numerical simulations are in close agreement. This agreement confirms the accuracy of the established finite element model of the bridges.

Additionally, a comparative analysis was conducted between the measured and simulated displacement time-history curves of the identical bridge during the train's passage. However, achieving complete consistency between the vehicle parameters of the simulated train and those of the actual operational train poses significant challenges. This is due to the operational freight trains, whose load weights are typically unknown and whose speeds may not be constant. Moreover, real measured data often contains noise interference, making it difficult to perfectly align the measured and simulated results.

Taking into consideration that freight trains often operate empty, a simulation model of the C62 freight train (comprising a DF4 locomotive and 20 empty C62 cars) is established. After investigating the approximate speed of the freight train passing through this curved bridge (at 35 km/h), the lateral displacement response at the midspan of a 24 m simply supported beam bridge is computed. This simulated data is then compared with the displacement response obtained from the same bridge point during the actual passage of the train, as shown in Figures 9 and 10. It is apparent that the two responses in the time and frequency domains are largely consistent, affirming the effectiveness of the numerical simulation model.

3. Efficient Performance Prediction Method

3.1. Performance Evaluation Metric. In order to assess the dynamic performance of bridges on small-radius reverse curves, a performance evaluation criterion must be devised. Critical indicators affecting bridge safety encompass the lateral displacement, lateral acceleration, and vertical acceleration at the midspan of the main beam and the top of bridge piers. Evaluation of whether these parameters meet safety requirements involves adherence to the railway bridge inspection specification of China [32], with specific threshold values or recommendations as follows:

(1) For situations where the train speed is less than 80 km/h, the recommended maximum lateral displacement at the midspan of a concrete bridge is defined by

$$A_{\max} \leq \frac{L}{7B_2}, \tag{11}$$

where L represents the calculated span of the bridge, and B_2 denotes either the transverse center-to-center distance of multi-girder systems or the spacing between supports.

For bridge piers with pile foundations, the suggested maximum lateral displacement can be expressed as follows:

$$A_{\max} \leq \frac{(H + \Delta h)^2}{100B_2} + 0.2, \tag{12}$$

where the corrected height Δh accounts for soil characteristics.

(2) The lateral acceleration of bridges is limited to 1.4 m/s^2.

(3) The vertical acceleration of bridges is restricted to 3.5 m/s^2.

These standards, derived from the railway bridge inspection specification, guide the assessment of lateral displacement, lateral acceleration, and vertical acceleration in order to ensure the safety of bridges situated on small-radius reverse curves. Compliance with the specification is pivotal in enhancing the dynamic performance and safety of such structures.

Table 1: Comparison of modal results between numerical simulation and field measurements.

Span (m)	Natural frequency (Hz)						Modal displacement ratio between pier top and bottom		
	First-order vertical bending of main beam			First-order lateral bending of main beam					
	Simulation	Measurement	Error (%)	Simulation	Measurement	Error (%)	Simulation	Measurement	Error (%)
20	6.16	6.24	1.3	12.06	12.15	0.7	2.63	2.42	8.0
24	5.12	5.36	4.7	8.45	8.67	2.6	2.84	2.56	9.9

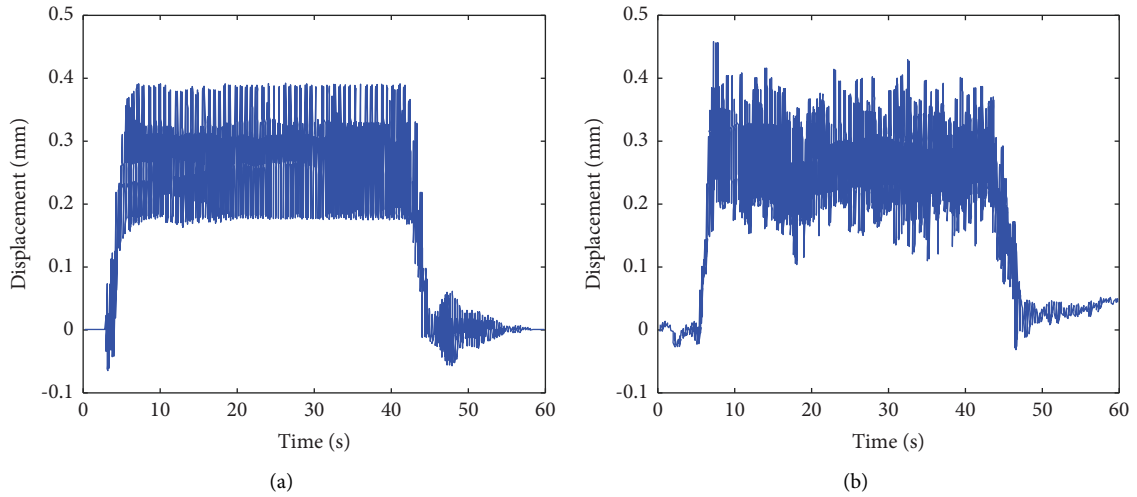

Figure 9: Time domain lateral displacement response at bridge midspan. (a) Numerical simulation. (b) Field measurement.

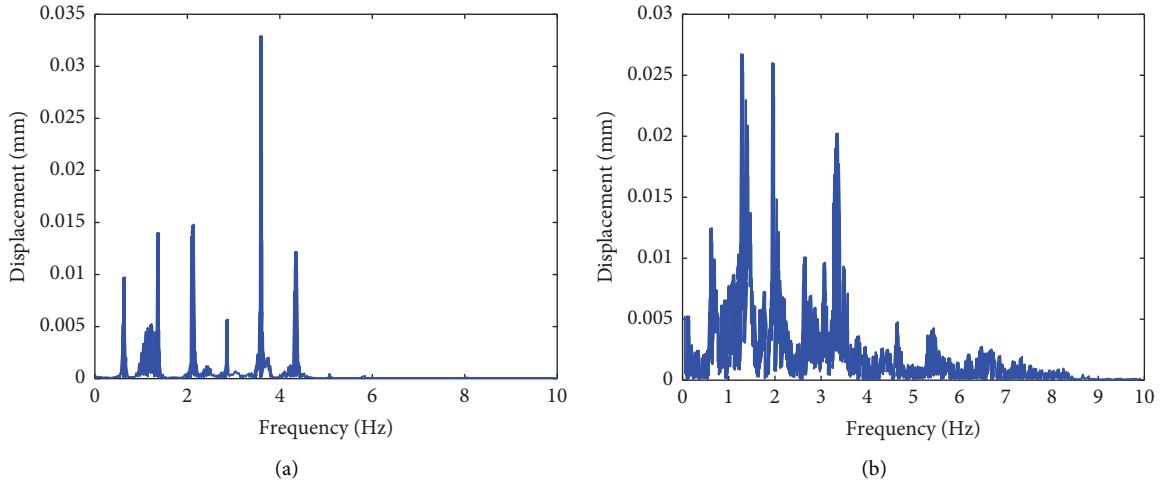

Figure 10: Frequency domain lateral displacement response at bridge midspan. (a) Numerical simulation. (b) Field measurement.

This paper introduces a comprehensive method for evaluating bridge dynamic performance based on the aforementioned threshold values. This approach integrates with labels used in classification tasks in machine learning, facilitating the direct prediction of the dynamic performance level of bridges through design parameters. Figure 11 illustrates the process of grading bridge dynamic performance using this comprehensive evaluation method. Initially, displacement and acceleration metrics for evaluating bridge dynamic performance are computed based on numerical simulation models, totaling four distinct metrics. The simulated values for these four metrics are calculated in relation to the limits or recommended values specified in regulations, measuring the surplus capacity of bridge dynamic performance. A higher proportion signifies a smaller surplus capacity in the bridge's dynamic performance. If the proportion exceeds 100%, it indicates a need for enhancement in the bridge's dynamic performance. Subsequently, the maximum value among these four proportions is selected, compared against the ratio intervals corresponding to the dynamic performance levels proposed in this study. Based on this comparison, the bridge is assigned its respective dynamic performance level. It is worth noting that these dynamic performance levels correspond to the labels used in the subsequent classification tasks.

3.2. Feature Selection. In order to directly predict the dynamic performance of bridges on small-radius reverse curves, it is crucial to select the most relevant and significant parameters from the multitude of variables. Feature selection serves to reduce computational costs, mitigate overfitting risks, and enhance the interpretability of computational outcomes. This study opts for design parameters closely linked to or directly correlated with dynamic responses as features. The selected parameters encompass (1) train speed, (2) bridge span, (3) pier height, (4) radius of the curve where the main beam is located,

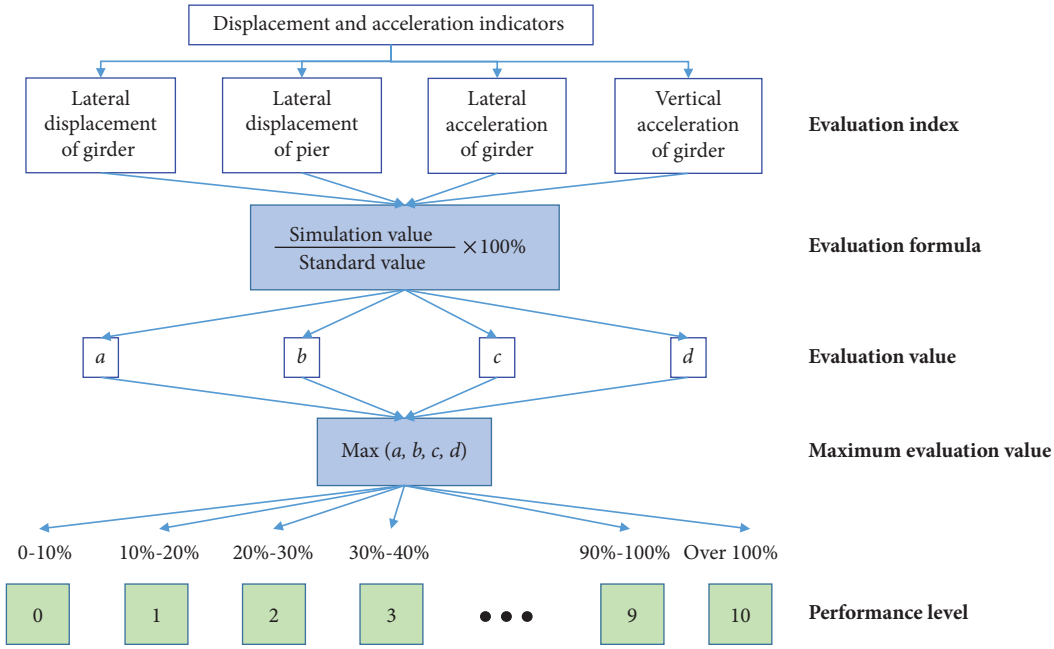

Figure 11: Determination of bridge dynamic performance level.

(5)–(7) first to third-order vertical natural frequency of the main beam, (8)–(10) First to third-order lateral natural frequency of the main beam, (11)–(13) first to third-order torsional natural frequency of the main beam, (14)–(16) first to third-order longitudinal natural frequency of the pier, (17)–(19) first to third-order lateral natural frequency of the pier, and (20)–(22) first to third-order torsional natural frequency of the pier.

To eliminate redundant features and undertake dimensionality reduction, principal component analysis (PCA) [33] is oftentimes employed. PCA is a classic statistical method that transforms correlated variables into a set of unrelated composite variables, or principal components. These new variables, obtained as linear combinations of the original variables, effectively reduce data dimensions. While PCA is capable of projecting high-dimensional data into a lower-dimensional space, preserving as much original data information as possible while reducing redundancy, it falls short in discerning the importance of original features (i.e., their contribution to machine learning model performance) due to the nature of feature mapping. To address this limitation, we turn to the Fisher Score method [34, 35] to quantify the distinctiveness between features, thereby further exploring which design parameters within the original set hold greater relevance for predicting bridge dynamic performance.

The Fisher score is a powerful technique used for reducing the dimensions of features in a dataset. Its primary objective is to identify a subset of features that, within a data space formed by these selected features, maximizes the distances between data points belonging to different classes while minimizing the distances between data points within the same class. Specifically, given a training dataset $X \in R^{m\times n}$ associated with c distinct classes, the Fisher score of the ith feature is calculated using the following equations [34, 35]:

$$\begin{aligned} \mathrm{FS}(f_i) &= \frac{S_b(f_i)}{\sum_{k=1}^{c} S_t^{(k)}(f_i)}, \\ S_b(f_i) &= \sum_{k=1}^{c} n_k\left(\mu_i^{(k)} - \mu_i\right)^2, \\ S_t^{(k)}(f_i) &= \sum_{j=1}^{n_k}\left(x_{ij}^{(k)} - \mu_i^{(k)}\right)^2, \end{aligned} \tag{13}$$

where $S_b(f_i)$ represents the between-class scatter of the ith feature, n_k stands for the number of samples in the kth class, $\mu_i^{(k)}$ denotes the mean of the ith feature within the kth class, μ_i signifies the mean of the ith feature in the dataset X, $S_t^{(k)}(f_i)$ represents the within-class scatter matrix of the ith feature related to the kth class, and $x_{ij}^{(k)}$ denotes the value of the ith feature for the jth sample in the kth class.

Higher Fisher scores indicate larger feature disparities between the classes, thus highlighting significant contributions for the dynamic performance prediction tasks in this study. In addition, reducing feature dimensions by selecting a small number of features associated with high Fisher Scores can enhance the training efficiency of classification models and mitigate the risk of overfitting.

3.3. Support Vector Machine. Support vector machine (SVM) [36] stands as a classical classification algorithm with the core objective of identifying the optimal classification

hyperplane when the sample data is linearly separable, as illustrated in Figure 12. The samples in proximity to the optimal hyperplane are termed support vectors, while the dashed lines parallel to the hyperplane and passing through these sample points represent the margin boundaries. SVM centers its focus on these support vector points, seeking to maximize the margin between the boundary lines through the identification of an optimal hyperplane.

Let $x \in R^n$ represent the feature vector data, and $y \in \{-1, 1\}$ denote the class labels. The discriminant function (hyperplane) can be expressed as $f(\mathbf{x}) = \omega\mathbf{x} + b$, where ω represents the weight vector normal to the hyperplane, and b is the bias term. At $f(\mathbf{x}) = 0$, the sample $\mathbf{x}$ lies on the classification hyperplane; when $f(\mathbf{x}) > 0$, $\mathbf{x}$ is classified under $y = 1$; and when $f(\mathbf{x}) < 0$, x falls within $y = -1$. Therefore, if $y(\omega\mathbf{x} + b) > 0$ holds for all samples $\mathbf{x}$, it implies correct classification for all samples.

Generally, the two margin boundaries on which the support vectors reside are defined as $\omega\mathbf{x} + b = \pm 1$. Consequently, the distance from a support vector to the classification hyperplane becomes $1/\|\boldsymbol{\omega}\|$, while the classification margin equates to $2/\|\boldsymbol{\omega}\|$. To maximize the classification margin of $2/\|\boldsymbol{\omega}\|$, and to facilitate optimization, this is often reformulated to minimize $(1/2)\|\boldsymbol{\omega}\|^2$. Thus, the SVM algorithm's objective function for discovering the optimal hyperplane is obtained as follows:

$$\begin{aligned} &\min \frac{1}{2}\|\boldsymbol{\omega}\|^2, \\ &\text{s.t., } y_i(\boldsymbol{\omega}\mathbf{x}_i + b) > 0, \quad i = 1, 2, \cdots, n. \end{aligned} \tag{14}$$

The standard approach for solving the objective function employs the Lagrange dual method. Initially, the objective function is transformed into Lagrange form:

$$L(\boldsymbol{\omega}, b, \boldsymbol{\alpha}) = \frac{1}{2}\|\boldsymbol{\omega}\|^2 - \sum_{i=1}^{n} \alpha_i \left(y_i(\boldsymbol{\omega}\mathbf{x}_i + b) - 1\right), \tag{15}$$

where $\alpha_i \geq 0$ represents Lagrange multipliers.

Taking derivatives of function L with respect to $\boldsymbol{\omega}$ and b, and setting them to zero, yields the following equation:

$$\begin{aligned} &\frac{\partial L}{\partial \boldsymbol{\omega}} = 0 \Longrightarrow \boldsymbol{\omega} = \sum_{i=1}^{n} \alpha_i y_i \mathbf{x}_i, \\ &\frac{\partial L}{\partial b} = 0 \Longrightarrow \sum_{i=1}^{n} \alpha_i y_i = 0. \end{aligned} \tag{16}$$

Thus, function L can be deduced as follows:

$$L(\boldsymbol{\omega}, b, \boldsymbol{\alpha}) = \sum_{i=1}^{n} \alpha_i - \frac{1}{2} \sum_{i,j=1}^{n} \alpha_i \alpha_j y_i y_j \mathbf{x}_i^T \mathbf{x}_j. \tag{17}$$

Ultimately, the optimization problem is formulated as follows:

$$\begin{aligned} &\max_{\alpha} \sum_{i=1}^{n} \alpha_i - \frac{1}{2} \sum_{i,j=1}^{n} \alpha_i \alpha_j y_i y_j \mathbf{x}_i^T \mathbf{x}_j, \\ &\text{s.t., } \alpha_i \geq 0 \, (i = 1, 2, \cdots, n), \sum_{i=1}^{n} \alpha_i y_i = 0. \end{aligned} \tag{18}$$

Through this, the algorithm can compute α that maximizes the objective function, thereby obtaining corresponding ω and b values, establishing the optimal classification hyperplane.

The aforementioned outlines the SVM algorithm's implementation for linearly separable datasets. However, in practical applications, many problems are not linearly separable. For such nonlinearly separable scenarios, a nonlinear mapping function is often employed to map the dataset into a higher-dimensional space, rendering it linearly separable in that space. This approach facilitates the construction of an SVM classifier to seek the optimal hyperplane. "It is noteworthy that this study utilizes the radial basis function kernel function in SVM to address nonlinearly separable scenarios effectively."

The original SVM method, initially designed for binary classification, has been adapted in this study using the one-vs-rest strategy for multiclass classification. This approach involves training individual binary classifiers for each class, designating the specific class as the positive class, and grouping the remaining classes as the negative class. During the prediction phase, these classifiers assign decision scores, and the class associated with the classifier yielding the highest score is selected as the ultimate predicted class. This strategic adoption efficiently transforms the multiclass problem into a sequence of binary decisions.

4. Results

This study utilizes a C62 freight train comprising 21 cars, inclusive of a DF4 locomotive, 10 loaded C62 cars, and 10 empty C62 cars. The speed conditions vary from 40 km/h to 80 km/h, increasing in increments of 10 km/h. The dynamic responses of the train passing through 80 simply supported beam bridges on small-radius curves are computed. Thus, the resulting dataset comprises 400 data samples. For each sample, the lateral displacement, lateral acceleration, and vertical acceleration at the midspan of the girder and the lateral displacement at the top of the pier are compared with the corresponding code limits or recommended values. The performance evaluation values, representing the proportions of simulation values to standard values, as discussed in

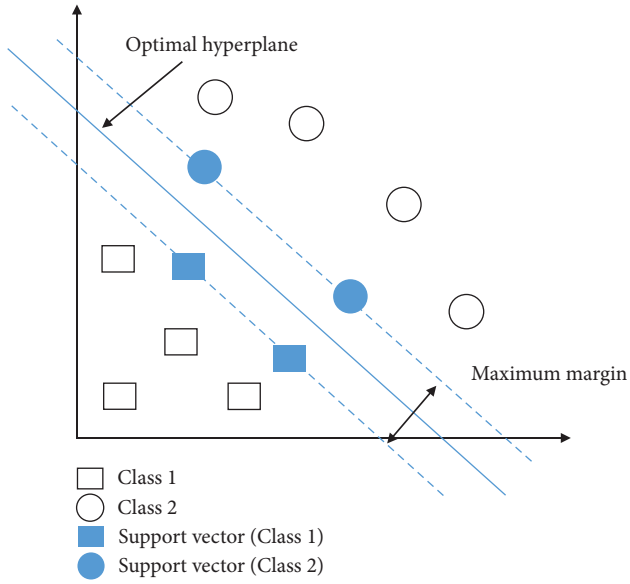

Figure 12: Support vector machine.

Section 3.1, are derived. Figure 13 displays the maximum evaluation values for all bridges under the five train speed conditions.

Observing Figure 13 reveals that, with the exception of certain bridges under the 70 km/h and 80 km/h train speeds, where the evaluation values surpass 100%, all other bridges meet the specified limit requirements. Considering that the actual operating speeds of freight trains on this curve line typically do not exceed 60 km/h, the dynamic performance of all bridges meets the regulatory requirements. Further analysis of the dynamic performance computation results indicates that the majority of bridges exhibiting high evaluation values do so because the lateral displacement of the pier top increases with higher train speeds, often exceeding the recommended values stipulated in design codes. As a result, when designing curved bridges, enhancing the lateral and torsional stiffness of piers becomes crucial.

The 400 data samples are labeled from 0 to 10 according to the outcomes depicted in Figure 13 and in accordance with the dynamic performance levels proposed in Section 3.1. However, in this study, only 5 labels correspond to the data samples. The distribution of these labels is depicted in Figure 14. This figure highlights that label 8 constitutes the majority among all the labels, while label 6 holds the smallest proportion.

In this study, the predictive outcomes of bridge dynamic performance are evaluated across six distinct tasks based on different speed divisions, as outlined in Table 2. With the exception of the final task, which encompasses all speed conditions in both training and test sets with independent data, tasks 1–5 involve distinct speed conditions. Tasks 1–5 specifically evaluate the model's efficacy in handling diverse and unfamiliar vehicle speeds. Evidently, the first five tasks establish the sample ratio of 4 : 1 for the training and test sets based on the division of speed conditions. This same sample allocation ratio is maintained in the final task, where the training and test sets follow a 4 : 1 ratio, randomly selected from the entire dataset. These tasks primarily assess the predictive models' ability to generalize bridge dynamic performance from known to unknown train speeds, as well as the model's performance when trained and applied using data from identical train speeds. During the training phase, a 5-fold cross-validation technique is utilized to determine the optimal hyperparameters for the support vector machine (SVM). In the application phase, the SVM with optimal hyperparameters is employed on the test data to predict dynamic performance outcomes.

Figure 15 showcases the importance of various design parameters obtained through Fisher Score computation across the six tasks. The feature numbers correspond to the design parameter numbers in Section 3.2, ensuring consistency. The significance of different features remain consistent across various tasks, as illustrated by the average values depicted in Figure 15 across the six tasks. Notably, the top five contributing features to the predictive model's performance are features numbered 1, 17, 18, 8, and 4. They correspond to Train speed, First-order lateral natural frequency of the pier, Second-order lateral natural frequency of the pier, First-order lateral natural frequency of the main beam, and Radius of the curve where the main beam is located, respectively. This finding emphasizes the paramount importance of aligning these five crucial design parameters during the bridge design phase. In other words, if the predicted outcomes for bridge dynamic performance do not meet the regulatory requirements, adjusting these five design parameters should be considered the primary course of action.

Figure 16 illustrates the results of dynamic performance prediction utilizing features sorted by the Fisher Score. The figure clearly indicates that as the count of features increases, the predictive accuracy for all six tasks steadily enhances. Upon reaching eight features, the predictive accuracy has essentially reached the level of accuracy achieved using all features. This validates the effectiveness of the Fisher score in

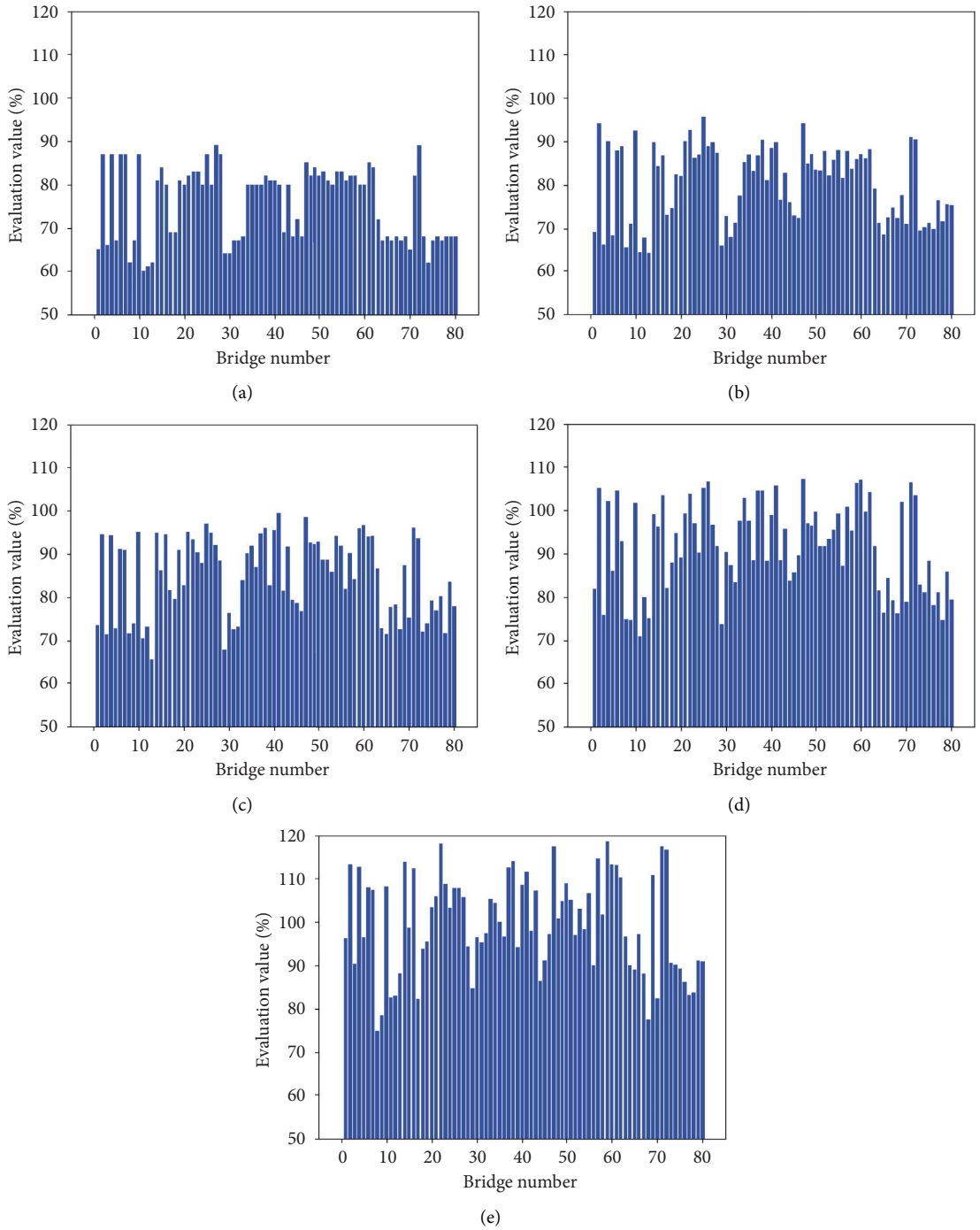

Figure 13: Maximum evaluation values for all bridges under five train speed conditions. (a) 40 km/h. (b) 50 km/h. (c) 60 km/h. (d) 70 km/h. (e) 80 km/h.

prioritizing feature importance for the predictive model and demonstrates its potential to reduce feature dimensions, thereby enhancing the training efficiency of the SVM model.

The highest predictive accuracy for bridge dynamic performance is 76.3% for Task 1, 79.2% for Task 2, 80.6% for Task 3, 81.1% for Task 4, and 75.0% for Task 5. For Task 6, the highest predictive accuracy reaches 86.9%, surpassing the results of Tasks 1 to 5. This disparity can be attributed to the fact that Tasks 1 and 2 involve training SVM models on data with known vehicle speeds and then applying them to data with unknown vehicle speeds. The bridge dynamic response data differ between the different vehicle speeds, leading to relatively poorer model test outcomes. In contrast, Task 6 encompasses training and testing sets that include data with all vehicle speeds, resulting in improved predictive outcomes compared to Tasks 1 to 5.

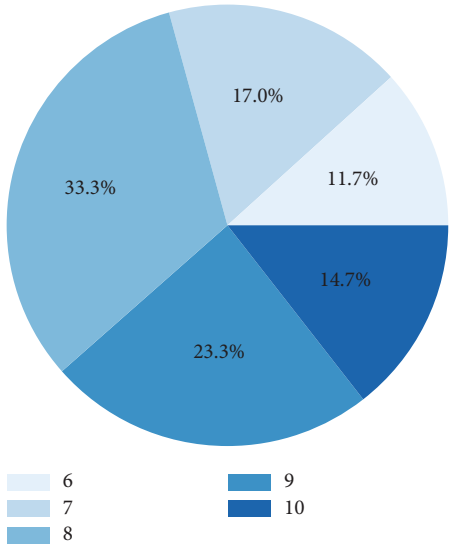

Figure 14: Distribution of data sample labels.

Table 2: Bridge dynamic performance prediction tasks.

Task	Training dataset (km/h)	Test dataset (km/h)
1	40, 50, 60, 70	80
2	40, 50, 60, 80	70
3	40, 50, 70, 80	60
4	40, 60, 70, 80	50
5	50, 60, 70, 80	40
6	40–80	40–80

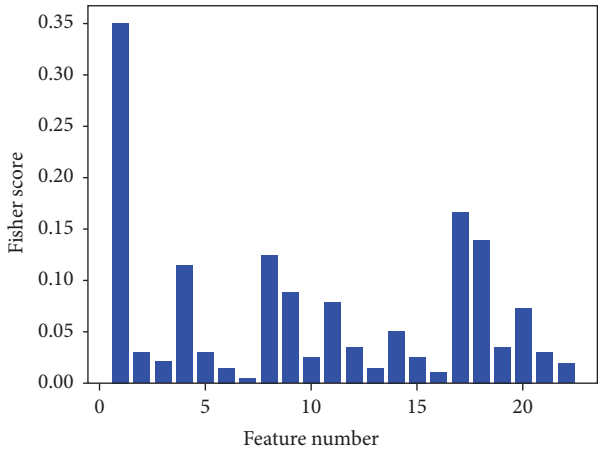

Figure 15: Relationship between feature number and fisher score.

The comparative results of these six tasks underscore the importance of comprehensively incorporating all operational conditions within the training set. Furthermore, the 86.9% predictive accuracy achieved in Task 6 highlights the effectiveness of the proposed method and its significant potential for application in the design of bridges on small-radius curves. This method involves training a bridge dynamic performance prediction model based on established numerical simulation models. It directly provides predicted values for the dynamic performance level of similar bridges, facilitating the optimization of design parameters in the initial design phase. In addition, it allows for a rough but rapid safety assessment of already constructed bridges, saving significant costs and time required to establish vehicle-bridge coupled vibration analysis models.

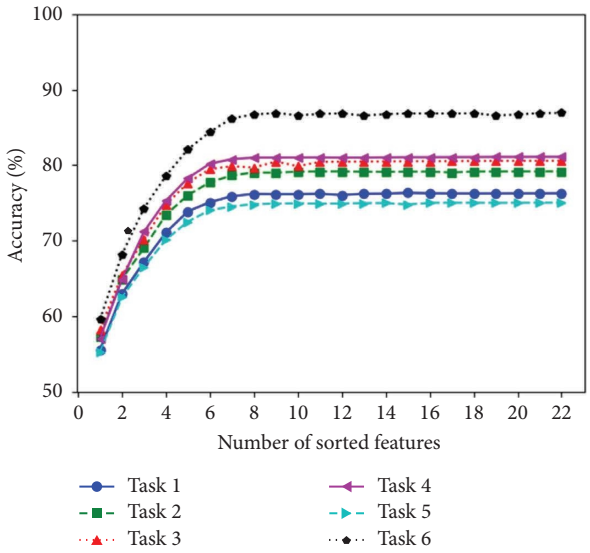

Figure 16: Predictive accuracy of bridge dynamic performance for different tasks.

5. Conclusion

This paper proposes an efficient method to predict the dynamic performance of bridges on small-radius reverse curves. By establishing a vehicle-bridge coupling vibration program based on train-curve bridge coupling vibration theory and conducting numerical simulation experiments, we generate ample a dynamic response data of bridges and label them with dynamic performance level. The bridge design parameters related to these dynamic response data are fed into a SVM to train a model that can directly predict the bridge's dynamic performance.

The outcomes reveal the highest predictive accuracy for bridge dynamic performance to be 86.9%, demonstrating the effectiveness of our proposed methodology and its potential utility in the design of bridges on small-radius curves. The relationship between feature number and Fisher score is also explored. Notably, the top five design parameters that significantly affect bridge dynamic performance prediction are train speed, first-order lateral natural frequency of the pier, second-order lateral natural frequency of the pier, first-order lateral natural frequency of the main beam, and radius of the curve where the main beam is located. These findings underscore the critical role of harmonizing these parameters during the bridge design process. When predicted bridge dynamic performance falls short of safety standards, prioritizing adjustments to parameters directly related to these five parameters is recommended.

The results from our study underscore the potential of our approach for facilitating the design and evaluation of bridges, particularly those located on small-radius curves. As the railway industry continues to evolve, our research contributes valuable insights into the fast optimization of bridge designs, ultimately ensuring safer and more efficient railway systems.

Data Availability

Data are available upon request.

Conflicts of Interest

The authors declare that they have no conflicts of interest.

Acknowledgments

The author would like to gratefully acknowledge the financial support from the Fund of State Key Laboratory of Bridge Engineering Structural Dynamics and Key Laboratory of Bridge Earthquake Resistance Technology, Ministry of Communications, PRC (E2(2022) No. 001).

References

[1] Q. He, C. Cai, S. Zhu, M. Wang, K. Wang, and W. Zhai, "Key parameter selection of suspended monorail system based on vehicle–bridge dynamical interaction analysis," *Vehicle System Dynamics*, vol. 58, no. 3, pp. 339–356, 2019.

[2] Y. Tian, L. Wang, and J. Zhang, "Time-varying frequency-based scaled flexibility identification of a posttensioned concrete bridge through vehicle–bridge interaction analysis," *Structural Control and Health Monitoring*, vol. 28, no. 1, Article ID e2631, 2021.

[3] F. Gong, F. Han, Y. Wang, and Y. Xia, "Bridge damping extraction method from vehicle–bridge interaction system using double-beam model," *Applied Sciences*, vol. 11, no. 21, Article ID 10304, 2021.

[4] Y. Song, G. Lin, F. Ni, J. Xu, and C. Chen, "Study on coupled vertical vehicle-bridge dynamic performance of medium and low-speed maglev train," *Applied Sciences*, vol. 11, no. 13, p. 5898, 2021.

[5] L. F. Fadel Miguel and G. Piva dos Santos, "Optimization of multiple tuned mass dampers for road bridges taking into account bridge-vehicle interaction, random pavement roughness, and uncertainties," *Shock and Vibration*, vol. 2021, Article ID 6620427, 17 pages, 2021.

[6] K.-H. Chu, C. L. Dhar, and V. K. Garg, "Railway-bridge impact: simplified train and bridge model," *Journal of the Structural Division*, vol. 105, no. 9, pp. 1823–1844, 1979.

[7] G. Diana and F. Cheli, "Dynamic interaction of railway systems with large bridges," *Vehicle System Dynamics*, vol. 18, no. 1-3, pp. 71–106, 1989.

[8] J. P. Yang and B.-L. Chen, "Rigid-mass vehicle model for identification of bridge frequencies concerning pitching effect," *International Journal of Structural Stability and Dynamics*, vol. 19, no. 02, Article ID 1950008, 2019.

[9] M. Yazdani and P. Azimi, "Assessment of railway plain concrete arch bridges subjected to high-speed trains," *Structures*, vol. 27, pp. 174–193, 2020.

[10] Y.-B. Yang and B.-H. Lin, "Vehicle-bridge interaction analysis by dynamic condensation method," *Journal of Structural Engineering*, vol. 121, no. 11, pp. 1636–1643, 1995.

[11] Q. Zeng and E. G. Dimitrakopoulos, "Vehicle–bridge interaction analysis modeling derailment during earthquakes," *Nonlinear Dynamics*, vol. 93, no. 4, pp. 2315–2337, 2018.

[12] Q. Li, Y.-L. Xu, D. Wu, and Z. Chen, "Computer-aided nonlinear vehicle-bridge interaction analysis," *Journal of Vibration and Control*, vol. 16, no. 12, pp. 1791–1816, 2010.

[13] E. Erduran, C. Nordli, and S. Gonen, "Effect of elastomeric bearing stiffness on the dynamic response of railway bridges considering vehicle–bridge interaction," *Applied Sciences*, vol. 12, no. 23, Article ID 11952, 2022.

[14] Y. Dong, W. Zhang, A. Shamsabadi, L. Shi, and E. Taciroglu, "A vehicle–bridge interaction element: implementation in ABAQUS and verification," *Applied Sciences*, vol. 13, no. 15, p. 8812, 2023.

[15] X. He, H. Qin, W. Liu, Y. Frank Chen, J. Zhai, and L. Yu, "Design, analysis and construction of a steel truss cable-stayed bridge for high-speed railway in China," *Structural Engineering International*, vol. 26, no. 4, pp. 381–388, 2016.

[16] L. Sun and X. Zhao, "Coupled dynamics of vehicle-bridge interaction system using high efficiency method," *Advances in Civil Engineering*, vol. 2021, Article ID 1964200, 22 pages, 2021.

[17] H. Yu, B. Wang, Y. Li, Y. Zhang, and W. Zhang, "Road vehicle-bridge interaction considering varied vehicle speed based on convenient combination of Simulink and ANSYS," *Shock and Vibration*, vol. 2018, Article ID 1389628, 14 pages, 2018.

[18] Y. Shao, J. Brownjohn, C. Miao, and M. Wang, "A precise time-integration linear vehicle-bridge interaction method and dynamic sensitivity analysis," *Structures*, vol. 33, pp. 4596–4603, 2021.

[19] Y. Zhang, W. Li, Z. Ji, and G. Wang, "Vehicle ride comfort analysis based on vehicle-bridge coupled vibration," *Shock and Vibration*, vol. 2021, Article ID 5285494, 14 pages, 2021.

[20] N. D. Lagaros and M. Papadrakakis, "Neural network based prediction schemes of the non-linear seismic response of 3D buildings," *Advances in Engineering Software*, vol. 44, no. 1, pp. 92–115, 2012.

[21] A. Joghataie and M. Farrokh, "Dynamic analysis of nonlinear frames by Prandtl neural networks," *Journal of Engineering Mechanics*, vol. 134, no. 11, pp. 961–969, 2008.

[22] H. Dongmei, H. Shiqing, H. Xuhui, and Z. Xue, "Prediction of wind loads on high-rise building using a BP neural network combined with POD," *Journal of Wind Engineering and Industrial Aerodynamics*, vol. 170, pp. 1–17, 2017.

[23] B. K. Oh, B. Glisic, Y. Kim, and H. S. Park, "Convolutional neural network-based wind-induced response estimation model for tall buildings," *Computer-Aided Civil and Infrastructure Engineering*, vol. 34, no. 10, pp. 843–858, 2019.

[24] H. Wang and T. Wu, "Knowledge-enhanced deep learning for wind-induced nonlinear structural dynamic analysis," *Journal of Structural Engineering*, vol. 146, no. 11, Article ID 04020235, 2020.

[25] H. Li, T. Wang, and G. Wu, "Dynamic response prediction of vehicle-bridge interaction system using feedforward neural network and deep long short-term memory network," *Structures*, vol. 34, pp. 2415–2431, 2021.

[26] H. Xiang, P. Tang, Y. Zhang, and Y. Li, "Random dynamic analysis of vertical train–bridge systems under small probability by surrogate model and subset simulation with splitting," *Railway Engineering Science*, vol. 28, no. 3, pp. 305–315, 2020.

[27] B. K. Oh, B. Glisic, S. W. Park, and H. S. Park, "Neural network-based seismic response prediction model for building structures using artificial earthquakes," *Journal of Sound and Vibration*, vol. 468, Article ID 115109, 2020.

[28] F. Mete, Y. Chen, A. Stathopoulos, and D. J. Corr, "Comparative study of predictive analysis methods to estimate bridge response," *Transportation Research Record*, vol. 2673, no. 9, pp. 365–376, 2019.

[29] S. C. Yang and S. H. Hwang, "Train-track-bridge interaction by coupling direct stiffness method and mode superposition method," *Journal of Bridge Engineering*, vol. 21, no. 10, Article ID 04016058, 2016.

[30] F. Liu, J.-M. Battini, and C. Pacoste, "Assessment of hollow-core concrete floors against human-induced vibration," *Structural Engineering International*, vol. 31, no. 3, pp. 376–390, 2021.

[31] J. Liu, W. Qu, N. Nikitas, and Z. Ji, "Research on extending the fatigue life of railway steel bridges by using intelligent control," *Construction and Building Materials*, vol. 168, pp. 532–546, 2018.

[32] China MoRotPsRo, *Code for Rating Existing Railway Bridge*, China Railway Publishing House, Beijing, China, 2004.

[33] H. Abdi and L. J. Williams, "Principal component analysis," *WIREs Computational Statistics*, vol. 2, no. 4, pp. 433–459, 2010.

[34] L. Sun, T. Wang, W. Ding, J. Xu, and Y. Lin, "Feature selection using Fisher score and multilabel neighborhood rough sets for multilabel classification," *Information Sciences*, vol. 578, pp. 887–912, 2021.

[35] X. He, D. Cai, and P. Niyogi, "Laplacian score for feature selection," *Advances in Neural Information Processing Systems*, vol. 18, 2005.

[36] M. A. Hearst, S. T. Dumais, E. Osuna, J. Platt, and B. Scholkopf, "Support vector machines," *IEEE Intelligent Systems and Their Applications*, vol. 13, no. 4, pp. 18–28, 1998.